

is carried out using the algorithms described in [10]. The second step, i.e., ”optimize”, is to define an optimal control problem, optimizing over a set of parameters describing the ideal closed-loop MIMO transfer function adhering to industry-standard grid codes. To account for the variability of grid operating conditions, multiple cycles of P&O are carried out in equal intervals. Although the P&O algorithm works efficiently in the single-converter case, it requires coordination between each converter in the multi-agent setup.

Contributions

While existing decentralized estimation algorithms can theoretically operate in parallel at each point of common coupling (PCC), they rely on restrictive operational assumptions. Specifically, they require coordinated system identification (SysID) [17], [19], [20], multiple operating points [11], [12], not considering closed-loop control interactions [16], or the unrealistic assumption of a perfectly stiff equivalent voltage (i.e., an infinite bus) [10], [14], [16], [18]. These assumptions frequently break down in dynamic, multi-agent networks.

To overcome these limitations and enable robust identification under active grid conditions, we propose a gray-box identification algorithm with the following primary contributions:

- 1) **Fully decentralized execution:** Our algorithm operates independently from each VSC using strictly local PCC measurements, requiring zero communication or coordinated timing with the rest of the grid. This inherent decoupling makes the approach highly scalable to grids of arbitrary sources and/ or loads.
- 2) **Separating active & passive entities:** From the perspective of the local VSCs, the algorithm extracts the parametric equivalent grid impedance and the non-parametric equivalent grid voltage. By executing this estimation in the frequency domain and using instrumental variables (IV), it is possible to decouple the physical transmission line dynamics from the active control reactions of other VSCs and loads, thus, resolving the severe cross-coupling errors that corrupt time-domain identification.
- 3) **Robustness:** Simulation results validate the algorithm’s accuracy using continuous, minimally invasive, wide-band excitations. Our method accurately identifies grid parameters despite non-ideal conditions, i.e., a low-inertia grid (not a rigid infinite bus), multi-agent simultaneous excitations, deviations in nominal amplitude and frequency, heterogeneous lines, and harmonic noise.

Outline

The rest of this paper is structured as follows: Section II describes the modeling and the formal problem statement. Section III describes the measurements recorded, grid-equivalent map, frequency discrimination (FD), and the algorithm to identify the grid-equivalent model. We show the simulation results on a 5-converter network in Section IV.

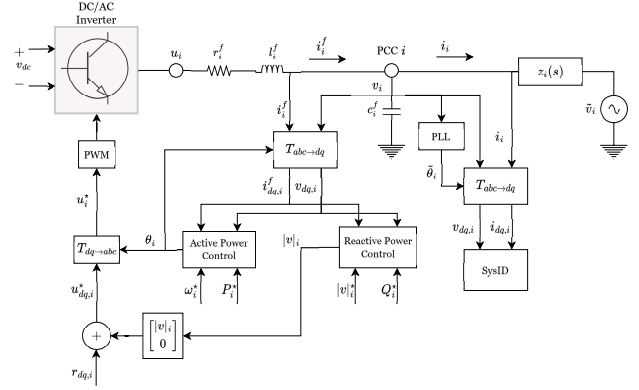


Fig. 2. Grid-forming control scheme considered in our work [21]. Note that the equivalent voltage \tilde{v}_i is not considered to be a rigid infinite bus.

Section V concludes our work and presents potential future directions.

Notations

We denote $s = j\omega$ as the transfer function variable. We denote $\mathbb{C}, \mathbb{C}^{n \times n}$ to be a complex number and an $n \times n$ complex matrix, respectively, and $\mathbb{R}_{\geq 0}^n, \mathbb{R}^n$ to be a non-negative and a general real-valued vector of dimension n , respectively. For any complex number $z \in \mathbb{C}$, $\Re\{z\}, \Im\{z\}$ denotes the real and imaginary parts of z , respectively. We let the quantity $[N]$ denote the set $\{1, 2, \dots, N\}$. We denote the quantity z^* to be the complex conjugate of z . We generate Gaussian distributed scalars (vectors) using $\mathcal{N}(a, b)$, where, a represents the mean (mean vector) and b represents the variance (covariance matrix). The expectation operator is denoted by $\mathbb{E}[\cdot]$. We denote $\|x\|$ to be the Euclidean norm and $\|x\|_S^2 := x^\top S x$. We denote the p^{th} entry of a vector x as $[x]_p$.

II. PROBLEM SETUP

In this section, we discuss the grid-connected converter model, the small-signal network dynamics, and present our estimation problem.

A. Grid-connected Converter Model

Fig. 2 shows the three-phase converter control design considered in our work. The converters are developed in grid-forming (GFM) mode [21] with droop control, although other GFM control strategies can also be used without any loss of generality.

A DC-AC inverter transforms power from the DC source with voltage $v_{dc,i}$ into a three-phase AC sinusoidal voltage u_i with the help of pulse-width modulation that dictates the frequency of switching of the inverter. We use an LC-filter at the converter side to smoothen the sinusoids. The filter dynamics (in three-phase) is given by:

$$\frac{d}{dt} i_i^f = \frac{1}{l_i^f} u_i - \frac{1}{l_i^f} v_i - \frac{r_i^f}{l_i^f} i_i^f, \quad \frac{d}{dt} v_i = \frac{1}{c_i^f} (i_i^f - i_i), \quad (1)$$

where i_i^f, i_i are the currents injected through the filter and at PCC i , respectively, u_i, v_i are the voltages at the output of the DC-AC inverter and at PCC i , respectively. The filter inductance, resistance, and capacitance are given by l_i^f, r_i^f, c_i^f , respectively.

The filter current i_i^f and PCC voltage v_i are then converted to their synchronous rotating reference frame (dq coordinates) using the Park transform [22, Chapter 3.3]

$$i_{dq,i}^f = T_{abc \rightarrow dq0}(\theta_i) i_i^f, v_{dq,i} = T_{abc \rightarrow dq0}(\theta_i) v_i, \quad (2)$$

where θ_i is the instantaneous angle at the converter side. The instantaneous active and reactive powers $P_i = \frac{3}{2} v_{dq,i}^\top i_{dq,i}^f$, $Q_i = \frac{3}{2} v_{dq,i}^\top J i_{dq,i}^f$, are computed, respectively, with $J = \begin{bmatrix} 0 & -1 \\ 1 & 0 \end{bmatrix}$. The instantaneous active and reactive powers are then passed through low-pass filters:

$$\frac{d}{dt} P_{i, \text{filt}} = \omega_i^c (P_i - P_{i, \text{filt}}) \ \& \ \frac{d}{dt} Q_{i, \text{filt}} = \omega_i^c (Q_i - Q_{i, \text{filt}}),$$

where, ω_i^c is the cut-off frequency for droop control. The droop control laws for voltage frequency and magnitude are then given by:

$$\omega_i = \omega_i^* - k_i^\omega (P_{i, \text{filt}} - P_i^*), |v|_i = |v|_i^* - k_i^v (Q_{i, \text{filt}} - Q_i^*), \quad (3)$$

respectively, where, $\omega_i, |v|_i$ are the voltage frequency and magnitude, respectively, with $\omega_i^*, |v|_i^*$ being their desired reference point, and k_i^ω, k_i^v are the tunable droop control parameters. Further, P_i^*, Q_i^* are the desired active and reactive power references, respectively. We then compute the angle at the converter side using the relation $\frac{d}{dt} \theta_i = \omega_i$, which is used in the abc to dq transformation matrix in (2).

The pulse-width modulation (PWM) signal in the dq coordinates is given by $u_{dq,i}^* = \begin{bmatrix} |v|_i^* \\ 0 \end{bmatrix} + r_{dq,i}$, where, $r_{dq,i}$ is an excitation signal for the purpose of estimation. We approximate the dynamics of the DC-AC inverter using the "average-value model", thus stating $u_i \approx T_{dq0 \rightarrow abc}(\theta_i) [(u_{dq,i}^*)^\top \ 0]^\top$, with $T_{dq0 \rightarrow abc}(\theta_i) = T_{abc \rightarrow dq0}(\theta_i)^{-1}$.

At each PCC, we record the current injected and the voltage in the dq coordinates, i.e., $i_{dq,i}, v_{dq,i}$, respectively. The conversion from abc to dq coordinates is carried out using the grid-angle measured using a phase-locked loop (PLL).

B. Small-signal Network Model

In this work, we consider a network of multiple three-phase voltage source converters (VSC) (as nodes of the network) interconnected with one another via transmission lines (as edges of the network) of non-zero impedance, as shown in Fig. 1. The dynamic small-signal model between PCC i and j in the dq coordinates [9] is given by $i_{dq,ij}(s) = y_{ij}(s)(v_{dq,i}(s) - v_{dq,j}(s))$, where, $i_{dq,ij}$ is the current from converter i to j , $y_{ij}(s) = x_{ij}(s)^{-1} \in \mathbb{C}^{2 \times 2}$ is the admittance (inverse of impedance) of the transmission line between i, j and $v_{dq,i}(s), v_{dq,j}(s)$ are the voltages at the

(PCC) generated by converters i, j , respectively. The current injection at each PCC i in a network of N converters is given by $i_{dq,i}(s) = \sum_{j=1, j \neq i}^N i_{dq,ij}(s)$. We now make the following assumption on the interconnection lines between the VSCs:

Assumption 1 (Line impedances). *The interconnecting line impedances have the following properties:*

- (i) *All interconnecting lines are resistive-inductive.*
- (ii) *Further, the lines are homogeneous, i.e. $\rho_{ij} = r_{ij}/l_{ij} = \rho, \forall i, j \in [N]$ (r_{ij}, l_{ij} in p.u.)*

Assumption 1(i) is commonly used in the power systems literature [9], [17], [18]. Assumption 1(ii) is used merely to fix a parametric structure on the impedance, and is not a hard requirement. Our algorithm works efficiently for heterogeneous networks as well.

Using Assumption 1, we have the following small-signal network model in dq coordinates [9]:

$$\begin{bmatrix} \Delta i_{dq,1}(s) \\ \Delta i_{dq,2}(s) \\ \vdots \\ \Delta i_{dq,N}(s) \end{bmatrix} = \Gamma \otimes y_\rho(s) \begin{bmatrix} \Delta v_{dq,1}(s) \\ \Delta v_{dq,2}(s) \\ \vdots \\ \Delta v_{dq,N}(s) \end{bmatrix}, \quad (4)$$

where, $\Delta i_{dq,i} = i_{dq,i} - i_{dq,i}^{ss}$ and $\Delta v_{dq,i} = v_{dq,i} - v_{dq,i}^{ss}$ refer to the deviations of the current and voltage at PCC i from their steady-state value, \otimes refers to the Kronecker product and the Laplacian matrix Γ is given by:

$$\Gamma = \begin{bmatrix} \sum_{j=1}^N \gamma_{1j} & -\gamma_{12} & \cdots & -\gamma_{1N} \\ -\gamma_{21} & \sum_{j=1}^N \gamma_{2j} & \cdots & -\gamma_{2N} \\ \vdots & \vdots & \ddots & \vdots \\ -\gamma_{N1} & -\gamma_{N2} & \cdots & \sum_{j=1}^N \gamma_{Nj} \end{bmatrix},$$

with $\gamma_{ij} = 1/l_{ij}$ (in p.u.). Finally, we have $y_\rho(s) = \frac{1}{1+(\rho+\frac{s}{\omega_b})^2} \begin{bmatrix} \rho + \frac{s}{\omega_b} & 1 \\ -1 & \rho + \frac{s}{\omega_b} \end{bmatrix}$, with ω_b being the nominal frequency of the grid.

C. Problem Statement

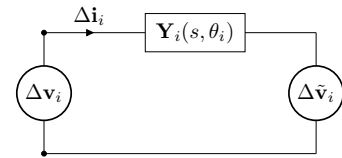


Fig. 3. Thevenin equivalent of Fig. 1 from the perspective of VSC i .

Consider the voltage and current injected at PCC i in the complex coordinates, i.e., $\Delta \mathbf{v}_i := \Delta v_{d,i} + j \Delta v_{q,i}$, $\Delta \mathbf{i}_i := \Delta i_{d,i} + j \Delta i_{q,i}$. For each converter $i \in [N]$, we look at the Thevenin equivalent (Fig. 3) model of the entire grid in the complex coordinates, which from (4) results in

$$\Delta \mathbf{i}_i(s) = \underbrace{\frac{\gamma_i}{s + j + \rho}}_{\mathbf{Y}_i(s)} (\Delta \mathbf{v}_i(s) - \Delta \tilde{\mathbf{v}}_i(s)), \quad (5)$$

where, $\gamma_i = \sum_{j=1}^N \gamma_{ij}$, and $\Delta \tilde{\mathbf{v}}_i(s) = \frac{1}{\gamma_i} \sum_{j=1}^N \gamma_{ij} \Delta \mathbf{v}_j(s)$ represents the small-signal equivalent voltage at PCC i in the complex coordinates.

Remark 1 (Complex coordinates). *Note that if the active (i.e., the equivalent voltage $\Delta \tilde{\mathbf{v}}_i(s)$) and passive (i.e., the equivalent admittance $\mathbf{Y}_i(s)$) entities were not distinguished, and a parametric approach was made to fit the overall equivalent model [10], [14], we would not have an SISO setup in (5), rather a 1×2 MIMO transfer function to be estimated [14].*

From VSC i 's perspective, it is desired to obtain a reliable representation of the entire equivalent grid, with only local information (i.e. $\Delta \mathbf{i}_i, \Delta \mathbf{v}_i$). The model parameters $\theta_i := [\rho \ \gamma_i]^\top$ and the small-signal equivalent grid voltage $\Delta \tilde{\mathbf{v}}_i$, are unknown. This leads to the following formal problem statement:

Problem 1. *Design a minimally invasive, decentralized gray box identification algorithm that estimates $\theta_i, \tilde{\mathbf{v}}_i \forall i \in [N]$ from each converter without interrupting grid operations, withstanding deviations from nominal conditions. Moreover, the algorithm should be able to be carried out in parallel across all converters.*

III. DECENTRALIZED IDENTIFICATION ALGORITHM

In this section, we propose a frequency domain approach to solve Problem 1. We discuss the measurements recorded, present the estimation framework, the frequency domain approach to estimation, and finally, present our algorithm.

A. Measurements

As seen in Fig. 2, at PCC i , we measure $i_{dq,i}, v_{dq,i}$, the local current and voltage, respectively in the dq coordinates, transformed with the angle measured using a PLL at the PCC. We then compute their deviations from their steady-state value¹ $\Delta i_{dq,i} = i_{dq,i} - i_{dq,i}^{ss}$ and $\Delta v_{dq,i} = v_{dq,i} - v_{dq,i}^{ss}$, respectively. The signals are then converted to their complex coordinate counterparts, i.e. $\Delta \mathbf{i}_i := \Delta i_{d,i} + j \Delta i_{q,i}$, $\Delta \mathbf{v}_i := \Delta v_{d,i} + j \Delta v_{q,i}$. We then sample these signals with a sampling frequency f_s and compute their fast Fourier transform (FFT) values² $\Delta \mathbf{i}_i(j\omega_k), \Delta \mathbf{v}_i(j\omega_k)$, at frequencies $\omega_k = 2\pi(f_s/N_s)k$, with f_s being the sampling frequency of the signals $\Delta \mathbf{i}_i, \Delta \mathbf{v}_i$ and N_s the total number of samples, and $k \in \{0, 1, 2, \dots, N_s\}$ the iteration count.

B. Grid-Equivalent Estimation Model Framework

We compute the ratio $h_i(j\omega_k) = \Delta \mathbf{i}_i(j\omega_k) / \Delta \mathbf{v}_i(j\omega_k)$ at each ω_k . Dividing both sides of (5) by $\mathbf{v}_i(j\omega_k)$, we obtain the following map

$$h_i(j\omega) = \mathbf{Y}_i(j\omega)(1 - \tilde{h}_i(j\omega)), \quad (6)$$

¹In the stochastic setting with multiple VSCs exciting simultaneously, the temporal mean at steady-state is considered as the steady-state value

²Note that although the estimation framework is in continuous-domain, we use the FFT as an approximation for the continuous-time Fourier transform, since the frequency response in continuous and its sampled discrete-time counterpart are identical for frequencies significantly lower than the Nyquist frequency.

where, $\mathbf{Y}_i(j\omega) = \frac{\gamma_i}{\rho + j(\omega+1)}$ is the equivalent admittance and $\tilde{h}_i(j\omega) = \Delta \tilde{\mathbf{v}}_i(j\omega) / \Delta \mathbf{v}_i(j\omega)$, the dynamic voltage coupling factor.

We then write h_i, \tilde{h}_i explicitly in terms of its real and imaginary components, i.e., $h_i(j\omega) = \mathbb{R}\{h_i(j\omega)\} + j\mathbb{I}\{h_i(j\omega)\}$, $\tilde{h}_i(j\omega) = \mathbb{R}\{\tilde{h}_i(j\omega)\} + j\mathbb{I}\{\tilde{h}_i(j\omega)\}$, respectively. Re-arranging the terms in (6), we obtain the following bilinear map

$$\underbrace{\begin{bmatrix} -(\omega+1)\mathbb{I}\{h_i(j\omega)\} \\ (\omega+1)\mathbb{R}\{h_i(j\omega)\} \end{bmatrix}}_{z_i(\omega)} = \underbrace{\begin{bmatrix} -\mathbb{R}\{h_i(j\omega)\} & 1 \\ -\mathbb{I}\{h_i(j\omega)\} & 0 \end{bmatrix}}_{H_i(\omega)} \underbrace{\begin{bmatrix} \rho \\ \gamma_i \end{bmatrix}}_{\theta_i} + \underbrace{\gamma_i}_{[\theta_i]_2} \underbrace{\begin{bmatrix} \mathbb{R}\{\tilde{h}_i(j\omega)\} \\ \mathbb{I}\{\tilde{h}_i(j\omega)\} \end{bmatrix}}_{d_i(\omega)}, \quad (7)$$

where, $\theta_i \in \mathbb{R}^2$ is the parameter vector of $\mathbf{Y}_i(j\omega)$ and is constant, while $d_i(\omega) \in \mathbb{R}^2$ represents the real and imaginary parts of the dynamic coupling with the grid \tilde{h}_i , and varies across frequencies.

With the model in (7), it is desired to estimate θ_i and $d_i(\omega_k)$, $\forall \omega_k \in \{0, 2\pi f_s/N_s, 4\pi f_s/N_s, \dots, \pi f_s/N_s\}$, for all converters $i \in [N]$ in a parallel and decentralized manner, leading to the following optimization problem

$$\arg \min_{\theta_i, \{d_i(\omega_k)\}_{k=0}^{N_s-1}} \sum_{k=1}^{N_s} \left\| z_i(\omega_k) - [H_i(\omega_k) \quad [\theta_i]_2] \begin{bmatrix} \theta_i \\ d_i(\omega_k) \end{bmatrix} \right\|_{R(\omega_k)}^2, \quad (8)$$

where, $R(\omega_k)$ is the measurement noise covariance of $z_i(\omega_k)$, and $\|x\|_S^2 := x^\top S x$.

Remark 2 (Non-convexity). *Since the estimation model (7) is bilinear in terms of θ_i, d_i , this results in the above optimization problem being non-convex. In addition, d_i varies across frequencies. Although the above problem has a feasible solution, a simultaneous estimation algorithm using gradient descent or recursive least-squares across frequency data points would yield sub-optimal results.*

Thus, we carry out the estimation of the overall equivalent model in two steps: (a) Parameter estimation by disregarding frequency points where the coupling $d_i(\omega)$ is significant, after which, (b) Equivalent voltage estimation is carried out. Before we explain the two-step estimation process, we offer the following justification to the gray-box framework that we have considered, i.e., a parametric and non-parametric setup for the equivalent admittance and voltage, respectively.

Remark 3 (Gray-box approach). *The equivalent admittance $\mathbf{Y}_i(s)$ represents a passive transmission line with a well-defined, low-order mathematical structure (resistive-inductive), making it convenient for parametric estimation. On the other hand, the dynamic coupling $\tilde{h}_i(j\omega)$ captures the lumped closed-loop reactions of all other VSCs in the grid. Since the exact control techniques (for example, GFM, grid-following, or the presence of high-inertia synchronous machines), along with numerous resonance frequency points*

of the filters of other VSCs are completely unknown, enforcing a parametric model on $h_{-i}(j\omega)$ would not be scalable. By estimating the coupling in a non-parametric manner, the local VSC can accurately map the grid's frequency-dependent stiffness without making restrictive assumptions about the grid. In addition, assuming an overall parametric model for the net equivalent impedance as in [10], [14] would not be applicable here since the grid is not assumed to be rigid and is realistically composed of other low-inertia sources that would excite simultaneously.

C. Parameter Estimation Algorithm

For the sake of parameter estimation, it must be noted that the small-signal equivalent voltage (and hence, $d_i(\omega)$ in (7)) $\Delta\tilde{\mathbf{v}}_i(s) = \frac{1}{\gamma_i} \sum_{m=1}^N \gamma_{im} \Delta\mathbf{v}_m(s)$ cannot be treated as a plain disturbance/ exogenous input. This is owing to the dependency on the PCC voltages of all other VSCs, which in turn, depend on the voltage at PCC i through the injected current, thus exhibiting a non-trivial closed-loop behaviour. Transients at the local PCC actively trigger the control loops of neighboring converters, causing the equivalent voltage $\Delta\tilde{\mathbf{v}}_i$ to be correlated with the local voltage $\Delta\mathbf{v}_i$. Standard least-squares estimation towards identifying $\mathbf{Y}_i(s)$ relies on the assumption that the input $\Delta\mathbf{v}_i$ is statistically independent of the "noise" ($\Delta\tilde{\mathbf{v}}_i(s)$ in this case). However, in our closed-loop setup, it is not the case: applying direct identification methods, such as ordinary least-squares or a raw empirical transfer function estimate (ETF) results in severe asymptotic bias (see Fig. 4 in Section IV for empirical evidence). The estimator absorbs the active control dynamics of the neighboring VSCs into the local admittance estimate, rendering the extraction of $\mathbf{Y}_i(s)$ highly inaccurate.

To minimize the closed-loop correlations, we employ instrumental variables (IV) in the frequency domain [23] by selecting the local wide-band excitation signal in the complex coordinates $\mathbf{r}_i = r_{d,i} + jr_{q,i}$ as the instrument. We now make an important assumption on the wide-band excitation signals of the VSCs.

Assumption 2 (Orthogonal excitations). *The wide-band excitations of all the VSCs are mutually orthogonal, i.e., $\mathbb{E}_{t \in \{0,1,2,\dots,N_s\}}[\mathbf{r}_i^*(t)\mathbf{r}_j(t)] \approx 0, \forall i, j \in [N], i \neq j$.*

Although the above assumption implies statistical independence of all the exciting signals \mathbf{r}_i , it does not require centralized communication. It is possible to guarantee orthogonality via the independent digital synthesis of excitation sequences at the microprocessors at each VSC, resulting in excitations that are almost always out of phase.

Pre-multiplying $\mathbf{r}_i(s)$ on both sides of (5) and taking the expectation, we obtain the following relation:

$$S_i^{RI}(j\omega) = \mathbf{Y}_i(j\omega)(S_i^{RV}(j\omega) - S_i^{R\tilde{V}}(j\omega)), \quad (9)$$

where, $S_i^{RI}(j\omega) = \mathbb{E}[\mathbf{r}_i^*(j\omega)\Delta\mathbf{i}_i(j\omega)]$, $S_i^{RV}(j\omega) = \mathbb{E}[\mathbf{r}_i^*(j\omega)\Delta\mathbf{v}_i(j\omega)]$ and $S_i^{R\tilde{V}}(j\omega) = \mathbb{E}[\mathbf{r}_i^*(j\omega)\Delta\tilde{\mathbf{v}}_i(j\omega)]$ represent the cross-spectral densities of the local wide-band

excitation \mathbf{r}_i with the small-signal current $\Delta\mathbf{i}_i$ and voltage $\Delta\mathbf{v}_i$ at PCC i , respectively, with $\mathbf{r}_i(j\omega)$ representing the FFT of $\mathbf{r}_i(t)$. By projecting the instrument \mathbf{r}_i onto the measured current and voltage via the cross-spectral density, we remove all uncorrelated noise. While \mathbf{r}_i still remains correlated with the grid voltage $\tilde{\mathbf{v}}_i$ due to the closed-loop effects (i.e., $\mathbb{E}[\mathbf{r}_i^*\tilde{\mathbf{v}}_i] \neq 0$), this pre-processing improves the possibility for the estimation to be separated between the passive admittance $\mathbf{Y}_i(j\omega)$ and the active contribution of the grid $\tilde{\mathbf{v}}_i$.

We compute the spectral densities, and hence, the ratio $h'_i(j\omega_k) = S_i^{RI}(j\omega_k)/S_i^{RV}(j\omega_k)$ at each ω_k . Henceforth, we replace ω_k with k for notational convenience. We then solve the following constrained least-squares problem:

$$\hat{\theta}_i = \arg \min_{\theta_i \in \mathbb{R}_{\geq 0}^2} \sum_{k=0}^{N_s} \left\| z'_i(k) - H'_i(k)\theta_i \right\|_{R_\theta(k)^{-1}}^2, \quad (10)$$

where, $z'_i(k) := \begin{bmatrix} -(\omega_k + 1)\Im\{h'_i(j\omega_k)\} \\ (\omega_k + 1)\Re\{h'_i(j\omega_k)\} \end{bmatrix}$ and $H'_i(k) := \begin{bmatrix} -\Re\{h'_i(j\omega_k)\} & 1 \\ -\Im\{h'_i(j\omega_k)\} & 0 \end{bmatrix}$ represents the output and $H_i(\omega)$ of our measurement model framework in (7), but with h_i being replaced by h'_i , $R_\theta(k) = \sigma_\theta(k)I_2$ is the measurement noise covariance associated with $z'_i(k)$. We set the measurement noise variance $\sigma_\theta(k) := c_1 + c_2(1 - \mathcal{W}_i(k))$, with $c_2 \gg c_1$. By setting $\mathcal{W}_i(k) = 0$, this informs the unreliability of frequency point ω_k towards parameter estimation. In this manner, we avoid the errors associated with frequency data points where the closed-loop effects from the rest of the grid exceeds that of the local VSC.

We now explain the frequency discrimination (FD) criteria (using a pseudo-code in Algorithm 1) to identify these unreliable frequency points (i.e., when $\mathcal{W}_i(k) = 0$) for parameter estimation.

- (A) **Coherence:** We compute the coherence factor $C_i^{RV}(k)$ between the local excitation \mathbf{r}_i and small-signal voltage $\Delta\mathbf{v}_i$, describing the linear dependence between them. If it is found to be lower than a given ϵ , the voltage response at that frequency is predominantly driven by the grid rather than the local VSC, and that data point is discarded.
- (B) **Band-pass filtering:** To prevent estimation bias from known physical operating conditions, we discard frequencies outside a bounded range $[\omega^a, \omega^b]$. Frequencies below ω^a are rejected as they are heavily dominated by the fundamental grid frequency (DC value in the dq and complex coordinates) and active closed-loop tracking dynamics (e.g., droop control, PLLs, etc.). Similarly, frequencies above ω^b are rejected to avoid spectral aliasing and high-frequency harmonics from the inverters.
- (C) **Passivity awareness:** Note that $\Re\{\mathbf{Y}_i(j\omega)\} > 0$ at all frequencies since $\gamma_i, \rho > 0$. Thus, if $\Re\{h'_i(j\omega)\} < 0$ at any frequency ω , it is certain that the noise (\tilde{h}_i in this case) completely overpowers that of the signal. We discard these frequencies for θ_i estimation.

Algorithm 1 Frequency Discrimination

$\mathcal{W}_i \leftarrow 1_{N_s}$ Frequency weight
for $k = 0$ **to** N_s **do**
 $C_i^{RV}(k) = |S_i^{RV}(j\omega_k)|^2 / (S_i^{RR}(j\omega_k)S_i^{VV}(j\omega_k))$
if $C_i^{RV}(k) < \epsilon$ **then** (A) Coherence
 $\mathcal{W}_i(k) \leftarrow 0$
end if
if $\omega_k < \omega^a$ OR $\omega_k > \omega^b$ **then** (B) Band-pass filtering
 $\mathcal{W}_i(k) \leftarrow 0$
end if
if $\Re\{h'_i(k)\} < 0$ **then** (C) Passivity awareness
 $\mathcal{W}_i(k) \leftarrow 0$
end if
end for

D. Small-signal Equivalent Voltage Estimation Algorithm

Upon estimating θ_i using (10), we now implement a Kalman filter algorithm [24] to estimate $d_i(k) \forall k \in \{0, 1, \dots, N_s\}$. The main idea is to treat this setup as an "unknown input observer" [25]. To this end, we define the process model as a random walk

$$d_i(k+1) = d_i(k) + q_i(k), \quad q_i(k) \sim \mathcal{N}(0_2, Q), \quad (11)$$

where, $d_i(k) := d_i(\omega_k)$ and process noise covariance $Q = \sigma_q I_2$.

The measurement model is given by $\tilde{z}_i(k) = [\hat{\theta}_i]_2 d_i(k) + \nu_i^d(k)$, with $\tilde{z}_i(k) = z_i(k) - H_i^\theta(k)\hat{\theta}_i$ and the measurement noise $\nu_i^d(k) \sim \mathcal{N}(0_2, R_d(k))$, with the measurement noise covariance $R_d(k) = c_1 I_2 + H_i(k)\Sigma_i H_i(k)^\top$, where Σ_i is the estimation covariance of θ_i .

We do not include process noise for the estimation of the parameters θ_i as they are fixed for linear time-invariant systems. On the other hand, d_i varies across frequency; thus, it is necessary to include a process noise.

Remark 4 (Process model). *In reality, there exists no deterministic model to describe the evolution of d_i along frequency data points. This intuitively prompts the process model to be $d_i(k) = q_i(k)$ rather than the random walk model in (11). However, given our hyper-parameter tuning, this leads to a high-gain observer, effectively resulting in a naive estimate $\hat{d}_i(k) \approx (H_i^d(k, \hat{\theta}_i))^{-1} \tilde{z}_i(k)$, which is heavily sensitive to small deviations in θ_i from its true value θ_i . Moreover, when there is no recursion in the process model, the algorithm does not learn from the errors of previous frequency data points.*

Similar to (10), we have the following optimization problem to solve for d_i :

$$\hat{d}_i(k) = \arg \min_{d_i(k)} \left\| \tilde{z}_i(k) - [\hat{\theta}_i]_2 d_i(k) \right\|_{R_d(k)^{-1}}^2 + \left\| d_i(k) - \hat{d}_i(k-1) \right\|_{Q^{-1}}^2, \quad (12)$$

leading to the following posterior update equations:

$$\hat{d}_i(k+1) = \hat{d}_i(k) + K_d(k)(\tilde{z}_i(k) - [\hat{\theta}_i]_2 \hat{d}_i(k)), \quad (13)$$

$$P_d(k+1) = (I_2 - [\hat{\theta}_i]_2 K_\theta(k))(P_d(k) + Q(k)), \quad (14)$$

with the Kalman filter gain at frequency iteration k given by

$$K_d(k) = [\hat{\theta}_i]_2 (P_d(k) + Q)(R_d + [\hat{\theta}_i]_2^2 (P_d(k) + Q))^{-1}.$$

Once d_i is estimated, it is then possible to ascertain the magnitude and phase of the small-signal equivalent voltage as $\Delta \tilde{\mathbf{v}}_i(j\omega) = \Delta \mathbf{v}_i(j\omega)([\hat{d}_i(j\omega)]_1 + j[\hat{d}_i(j\omega)]_2)$.

IV. NUMERICAL CASE STUDIES

In this section, we present the numerical values of the problem setup. Subsequently, we present the choice of hyperparameters, and then the simulation results of parameter and equivalent voltage estimation.

A. Experimental Setup

We consider an $N = 5$ converter system interconnected with each other via a resistive-inductive line. The parameter values considered are shown in Table I. The resistance and inductance value in p.u. between VSC i, j is given by $r_{ij} = R_{ij}/Z_b, l_{ij} = L_{ij}/L_b$ with their ranges as shown in Table I, with resistance-to-inductance ratio $\rho_{ij} = r_{ij}/l_{ij} \ll 1$ [9]. In addition, it is assumed that no two edges share the same ρ_{ij} , i.e., the lines are heterogeneous. Note that in the heterogeneous case, the true mathematical representation for equivalent admittance and small-signal voltage in (5) are $\mathbf{Y}_i(s) = \sum_{j=1, j \neq i}^N \frac{\gamma_{ij}}{s+j+\rho_{ij}}$ and $\Delta \tilde{\mathbf{v}}_i(s) = \frac{1}{\mathbf{Y}_i(s)} \sum_{j=1, j \neq i}^N \frac{\gamma_{ij}}{s+j+\rho_{ij}} \Delta \mathbf{v}_j(s)$, respectively, with $\rho_{ij} = r_{ij}/l_{ij}$.

We carry out 20 Monte-Carlo experiments with our 5-converter system. Across the experiments, although the line parameters remain constant, we consider different cut-off frequencies and droop control parameters in the VSCs, along with the excitation sequence varying across the experiments (see Table I for parameter ranges). Pseudo-random binary sequences (PRBS) of magnitude 0.001 p.u. are injected into the reference signal at each VSC (refer Fig. 2), in line with the specified grid codes for harmonics: IEEE 519 [26]. The initial phase angle for all converters is set to be zero.

TABLE I
PARAMETER VALUES OF THE GRID & CONVERTERS

Parameter	Symbol	Numerical value
Base power & frequency	S_b, ω_b	10kVA, 100π rad/s
Base voltage	v_b	380V
Base impedance, inductance	Z_b, L_b	$21.67\Omega, 0.067\text{H}$
Base capacitance	C_b	$150\mu\text{F}$
Resistance, Inductance (p.u.)	r_{ij}^f, l_{ij}^f	$[0.01, 0.03], [0.03, 0.3]$
Converter filter (p.u.)	r_i^f, l_i^f, c_i^f	$[0.01, 0.02], [0.03, 0.4], [0.015, 0.02]$
Cut-off frequency	ω_i^c	$2\pi[5, 10]$ rad/s
Droop control gains	k_i^w, k_i^v	$[2, 3] \times 10^{-5}, [2, 3] \times 10^{-4}$
References (p.u.)	ω_i^*, P_i^*, Q_i^*	$1, [0.9, 1.1], 0$
PRBS excitations (p.u.)	$r_{dq,i}$	$[0.999, 1.001]$

Remark 5 (Simultaneous excitations). *Note that for general SysID algorithms in the single converter case with an infinite*

bus, the larger the excitation magnitude (in this case, the PRBS $r_{dq,i}$), the better the estimation, for example, a magnitude of 0.1 p.u. in [10]. However, in our multi-agent setup, the grid voltage is not a rigid infinite bus. Thus, an increase in the excitation amplitude of one VSC, which would aid in the estimation of its equivalent model, would be detrimental to the estimation of other VSCs' equivalent impedance. Hence, it is vital that all VSCs strictly adhere to the grid code limitations on excitation amplitude.

We then measure the current and voltage at PCC i at a sampling rate $f_s = 10\text{kHz}$, with the total simulation time being $N_{total} = 81.6\text{s}$.

B. Hyperparameter Selection

While using the estimation model in (7), we carry out a double normalization at each frequency ω_k to avoid numerical issues at very low and high frequencies: (a) replacing ω_k with ω_k/ω_b and (b) dividing the left and right sides by $k_{norm}(\omega_k) = \max\{1, (\omega_k/\omega_b)\}$ in (7).

In the parameter estimation algorithm in Section III-C, we set the hyperparameters $c_1 = 0.1, c_2 = 10^{20}$, thus almost disregarding data points where the grid voltage corrupts data for parameter estimation. In the pseudo-code for frequency discrimination in Algorithm 1, we set $\epsilon = 0.05$ to disregard frequency points predominantly dominated by the grid, the band-pass cut-off frequencies $\omega^a = 150\text{ rad/s}$ and $\omega^b = 3000\text{ rad/s}$ to remove the biased data owing to the nominal grid operation and droop control in the lower frequencies, and aliasing errors in the higher frequencies, respectively.

C. Simulation Results

In Fig. 4, we show the raw ETFE along with the true equivalent admittance $\mathbf{Y}_i(s)$ from the perspective of VSC 1. At low frequencies³, the significant bias in the raw ETFE is due to the VSCs operating in the vicinity of the nominal frequency ω_b and the droop-control response of all VSCs to the PRBS excitation. On the other hand, the high-frequency noise peaks stem from capacitive resonances and aliasing issues as we get closer to the Nyquist rate ($\pi \times 10^4\text{ rad/s}$). We also note that there exists wide-band spectral noise at all frequencies owing to the simultaneous excitation of all VSCs. From Fig. 4, we see that in order to elegantly separate the estimation of \mathbf{Y}_i from the equivalent voltage $\Delta\tilde{\mathbf{v}}_i$, it is necessary to employ the frequency-domain pre-processing techniques described in Section III-C. We now describe the simulation results using our proposed algorithm. Fig. 5(a),(b) shows the resulting magnitude and phase plots for the equivalent transfer function estimated from the perspective of VSC 1 ($\mathbf{Y}_1(s)$), using the algorithm in Section III-C, respectively. We observe an average magnitude and phase error of 0.26 dB(3.13%) and 0.07 deg(0.08%), with a maximum

³Note that we have employed our algorithm in the complex domain after converting to the dq coordinates. Thus, low frequencies in the complex coordinate correspond to regions in the vicinity of the nominal operating frequency (i.e., ω_b) in the abc coordinates.

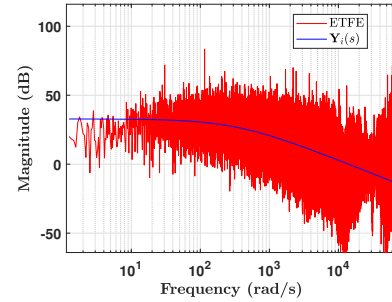


Fig. 4. A representative plot of the true equivalent admittance as seen from VSC 1 (blue) along with its ETFE counterpart (i.e. $|h_1(j\omega)| = |\Delta\mathbf{i}_1(j\omega)|/|\Delta\mathbf{v}_1(j\omega)|$)

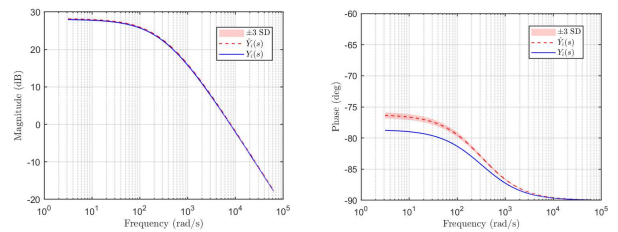


Fig. 5. Representative plots of the estimated (in hyphenated red) (a) (left) Magnitude ($|\mathbf{Y}_1(j\omega)|$) and (b) (right) Phase ($\angle\mathbf{Y}_1(j\omega)$) along with the true values (in blue), across 20 Monte-Carlo experiments. Note that the phase angle is non-zero at zero frequency owing to complex poles in $\mathbf{Y}_i(s)$. The shaded region in red denotes the ± 3 standard deviation across the experiments.

of 0.27 dB(3.2%) and 2.39 deg(3.04%), respectively. Upon estimating the parameters $\hat{\theta}_i$, we then carry out equivalent voltage estimation as explained in Section III-D. Note that Section III-D describes the estimation for the "small-signal" equivalent voltage $\Delta\tilde{\mathbf{v}}_i$. In order to compute the large-signal equivalent voltage $\tilde{\mathbf{v}}_i = \Delta\tilde{\mathbf{v}}_i + \tilde{\mathbf{v}}_i^{ss}$, it is required to compute and manually account for the steady-state/ DC value $\tilde{\mathbf{v}}_i^{ss}$. We compute the steady-state value using (5), i.e. $\hat{\tilde{\mathbf{v}}}_i^{ss} = \frac{1}{\hat{\mathbf{Y}}_i(j0)}(\mathbf{i}_i(j0) - \hat{\mathbf{Y}}_i(j0)\mathbf{v}_i(j0))$ using the estimated $\hat{\mathbf{Y}}_i$ from parameter estimation. We then show the results of magnitude estimation of the equivalent voltage in Fig. 6. We also show the corresponding estimation results in time-domain, by taking the inverse Fourier transform and separating into the d and q coordinates in Fig. 7(a) and (b), respectively.

V. CONCLUSIONS

We proposed a parallel and decentralized algorithm in the frequency domain for grid-equivalent model estimation from a local converter's perspective. To separate the local equivalent impedance from that of the equivalent grid voltage, we designed a bilinear mapping framework that dissolves into two separate estimation problems for equivalent parameter and grid voltage estimation using frequency-domain pre-processing techniques. We then used two estimation algorithms, a constrained least-squares and a Kalman filter to

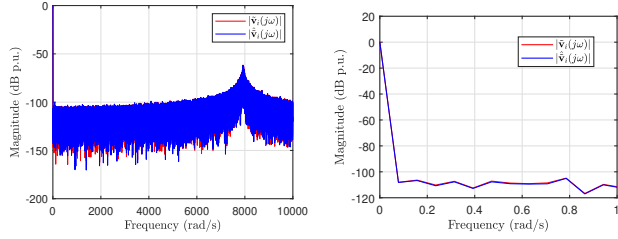


Fig. 6. Representative plots of the estimation of the equivalent voltage $|\hat{v}_i(j\omega)|$ at (a) (left) all frequencies and (b) (right) a close-up view on the lower frequency bins (corresponding to the region of nominal frequency ω_b in the abc coordinates). The red and blue plots denote the true and estimated values, respectively.

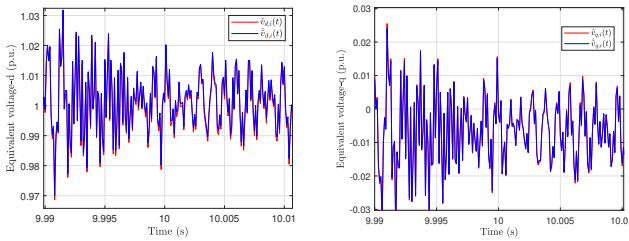


Fig. 7. Representative plots of the equivalent voltage in the (a) (left) d -coordinates and (b) q -coordinates. The red and blue plots denote the true and estimated values, respectively. The estimated $\hat{v}_{dq,i}(t)$ is obtained by taking the inverse Fourier transform of $\hat{v}_i(j\omega)$, after which, the real and imaginary parts are separated as the d and q coordinates.

estimate the parameters and the grid voltage, respectively, and showed promising results on an interconnected 5-converter system, all of them in grid-forming mode. Future compelling directions include applying the algorithm in a real-world setup; speeding up the estimation; stability analysis of the grid using the estimated model; including synchronous generators and other control techniques for converters (for example, virtual oscillator control, virtual synchronous machine, grid-following control schemes, etc.) in the simulations, and finally, designing decentralized adaptive control algorithms using the identified equivalent model.

REFERENCES

- [1] F. Milano, F. Dörfler, G. Hug, D. J. Hill, and G. Verbič, "Foundations and challenges of low-inertia systems (invited paper)," in *2018 Power Systems Computation Conference (PSCC)*, 2018, pp. 1–25.
- [2] D. Groß, M. Colombino, J.-S. Brouillon, and F. Dörfler, "The effect of transmission-line dynamics on grid-forming dispatchable virtual oscillator control," *IEEE Transactions on Control of Network Systems*, vol. 6, no. 3, pp. 1148–1160, 2019.
- [3] U. Markovic, O. Stanojevic, P. Aristidou, E. Vrettos, D. Callaway, and G. Hug, "Understanding small-signal stability of low-inertia systems," *IEEE Transactions on Power Systems*, vol. 36, no. 5, pp. 3997–4017, 2021.
- [4] J. Sun, "Impedance-based stability criterion for grid-connected inverters," *IEEE Transactions on Power Electronics*, vol. 26, no. 11, pp. 3075–3078, 2011.
- [5] C. Li, M. Molinas, O. B. Fosfo, N. Qin, and L. Zhu, "A data-driven approach to grid impedance identification for impedance-based stability analysis under different frequency ranges," in *2019 IEEE Milan PowerTech*, 2019, pp. 1–6.
- [6] M. Céspedes and J. Sun, "Online grid impedance identification for adaptive control of grid-connected inverters," in *2012 IEEE Energy Conversion Congress and Exposition (ECCE)*, 2012, pp. 914–921.
- [7] J. R. Massing and H. Pinheiro, "Adaptive current control of grid-connected vsc with lcl-filters using parallel feedforward compensation," in *IECON 2010 - 36th Annual Conference on IEEE Industrial Electronics Society*, 2010, pp. 3185–3191.
- [8] S. Liu, Y. Li, and J. Xiang, "An islanding detection method based on system identification," in *The 27th Chinese Control and Decision Conference (2015 CCDC)*, 2015, pp. 5515–5520.
- [9] V. Häberle, X. He, L. Huang, F. Dörfler, and S. Low, "Decentralized parametric stability certificates for grid-forming converter control," 2025. [Online]. Available: <https://arxiv.org/abs/2503.05403>
- [10] V. Haberle, L. Huang, X. He, E. Prieto-Araujo, R. S. Smith, and F. Dörfler, "Mimo grid impedance identification of three-phase power systems: Parametric vs. nonparametric approaches," in *2023 62nd IEEE Conference on Decision and Control (CDC)*, 2023, pp. 542–548.
- [11] S. Cobreces, E. J. Bueno, D. Pizarro, F. J. Rodriguez, and F. Huerta, "Grid impedance monitoring system for distributed power generation electronic interfaces," *IEEE Transactions on Instrumentation and Measurement*, vol. 58, no. 9, pp. 3112–3121, 2009.
- [12] J. Huang, K. A. Corzine, and M. Belkhatay, "Small-signal impedance measurement of power-electronics-based ac power systems using line-to-line current injection," *IEEE Transactions on Power Electronics*, vol. 24, no. 2, pp. 445–455, 2009.
- [13] G. Francis, R. Burgos, D. Boroyevich, F. Wang, and K. Karimi, "An algorithm and implementation system for measuring impedance in the d - q domain," in *2011 IEEE Energy Conversion Congress and Exposition*, 2011, pp. 3221–3228.
- [14] M. Abdalmoaty, V. Häberle, X. He, and F. Dörfler, "Ultrafast grid impedance identification in dq -asymmetric three-phase power systems," in *Arxiv Pre-print, arXiv:2510.12338*, 2025.
- [15] L. Ljung, *System Identification*. Boston, MA: Birkhäuser Boston, 1998, pp. 163–173.
- [16] A. Rezaeizadeh, S. Mastellone, F. Bertoldi, and P. A. Hokayem, "Structure and parameters estimation of complex grid impedance," in *2024 European Control Conference (ECC)*, 2024, pp. 1991–1996.
- [17] N. Mohammed, T. Kerekes, and M. Ciobotaru, "Communication-free equivalent grid impedance estimation technique for multi-inverter systems," *IEEE Transactions on Industrial Electronics*, vol. 70, no. 2, pp. 1542–1552, 2023.
- [18] N. Hoffmann and F. W. Fuchs, "Minimal invasive equivalent grid impedance estimation in inductive-resistive power networks using extended kalman filter," *IEEE Transactions on Power Electronics*, vol. 29, no. 2, pp. 631–641, 2014.
- [19] V. Häberle, X. He, L. Huang, E. Prieto-Araujo, and F. Dörfler, "Optimal dynamic ancillary services provision based on local power grid perception," *IEEE Transactions on Power Systems*, vol. 40, no. 2, pp. 1816–1831, 2025.
- [20] N. Mohammed, M. H. Ravanji, W. Zhou, and B. Bahrani, "Online grid impedance estimation-based adaptive control of virtual synchronous generators considering strong and weak grid conditions," *IEEE Transactions on Sustainable Energy*, vol. 14, no. 1, pp. 673–687, 2023.
- [21] N. Guruwacharya, S. Chakraborty, G. Saraswat, R. Bryce, T. M. Hansen, and R. Tonkoski, "Data-driven modeling of grid-forming inverter dynamics using power hardware-in-the-loop experimentation," *IEEE Access*, vol. 12, pp. 52 267–52 281, 2024.
- [22] P. S. Kundur, *Power System Stability and Control*. CRC Press, 2012.
- [23] M. Gilson, J. S. Welsh, and H. Garnier, "Frequency-domain instrumental variable based method for wide band system identification," in *2013 American Control Conference*, 2013, pp. 1663–1668.
- [24] R. E. Kalman, "A new approach to linear filtering and prediction problems," *Journal of Basic Engineering*, vol. 82, no. 1, pp. 35–45, 03 1960.
- [25] M. Darouach, M. Zasadzinski, and S. Xu, "Full-order observers for linear systems with unknown inputs," *IEEE Transactions on Automatic Control*, vol. 39, no. 3, pp. 606–609, 1994.
- [26] "Ieee standard for harmonic control in electric power systems," *IEEE Std 519-2022 (Revision of IEEE Std 519-2014)*, pp. 1–31, 2022.